ORIGINAL RESEARCH

Open Access

Impact of tissue transport on PET hypoxia quantification in pancreatic tumours

Edward Taylor[1,2]* , Jennifer Gottwald[1,3], Ivan Yeung[1,4], Harald Keller[1,4], Michael Milosevic[1,4], Neesha C. Dhani[1,5], Iram Siddiqui[6], David W. Hedley[1,3,5] and David A. Jaffray[1,2,3,4,7]

Abstract

Background: The clinical impact of hypoxia in solid tumours is indisputable and yet questions about the sensitivity of hypoxia-PET imaging have impeded its uptake into routine clinical practice. Notably, the binding rate of hypoxia-sensitive PET tracers is slow, comparable to the rate of diffusive equilibration in some tissue types, including mucinous and necrotic tissue. This means that tracer uptake on the scale of a PET imaging voxel—large enough to include such tissue *and* hypoxic cells—can be as much determined by tissue transport properties as it is by hypoxia. Dynamic PET imaging of 20 patients with pancreatic ductal adenocarcinoma was used to assess the impact of transport on surrogate metrics of hypoxia: the tumour-to-blood ratio [TBR(*t*)] at time *t* post-tracer injection and the trapping rate k_3 inferred from a two-tissue compartment model. Transport quantities obtained from this model included the vascular influx and efflux rate coefficients, k_1 and k_2, and the distribution volume $v_d \equiv k_1 / (k_2 + k_3)$.

Results: Correlations between voxel- and whole tumour-scale k_3 and TBR values were weak to modest: the population average of the Pearson correlation coefficients (*r*) between voxel-scale k_3 and TBR (1 h) [TBR(2 h)] values was 0.10 [0.01] in the 20 patients, while the correlation between tumour-scale k_3 and TBR(2 h) values was 0.58. Using Patlak's formula to correct uptake for the distribution volume, correlations became strong (*r* = 0.80[0.52] and *r* = 0.93, respectively). The distribution volume was substantially below unity for a large fraction of tumours studied, with v_d ranging from 0.68 to 1 (population average, 0.85). Surprisingly, k_3 values were strongly correlated with v_d in all patients. A model was proposed to explain this in which k_3 is a combination of the hypoxia-sensitive tracer binding rate k_b and the rate k_{eq} of equilibration in slow-equilibrating regions occupying a volume fraction $1 - v_d$ of the imaged tissue. This model was used to calculate the proposed hypoxia surrogate marker k_b.

Conclusions: Hypoxia-sensitive PET tracers are slow to reach diffusive equilibrium in a substantial fraction of pancreatic tumours, confounding quantification of hypoxia using both static (TBR) and dynamic (k_3) PET imaging. TBR is reduced by distribution volume effects and k_3 is enhanced by slow equilibration. We proposed a novel model to quantify tissue transport properties and hypoxia-sensitive tracer binding in order to improve the sensitivity of hypoxia-PET imaging.

Keywords: Positron emission tomography, Hypoxia imaging, PET tracer kinetic modelling

Background

Positron emission tomography imaging of hypoxia is a promising way to detect hypoxia non-invasively in solid tumours [1, 2]. A major challenge to this approach is that the binding rate of hypoxia-sensitive PET tracers such as fluoromisonidazole (FMISO) and

fluoroazomycinarabinoside (FAZA) is slow as compared to, e.g., flurodeoxyglucose (FDG), and can be comparable to diffusive equilibration rates in tumour tissues.

As an example, a typical threshold used to decide whether or not a PET voxel hypoxic is that the voxel-scale tracer concentration exceeds that in blood by 20% after 2 h; i.e.,TBR (2 h) >1.2 [3–5]. This means that the binding rate of tracer in hypoxic tissue is

$$k_b \gtrsim \frac{0.2}{2h} = 0.1 \ h^{-1}. \qquad (1)$$

*Correspondence: edward.taylor@rmp.uhn.ca
[1]Princess Margaret Cancer Centre, University Health Network, Toronto, Canada
[2]Techna Institute, University Health Network, Toronto, Canada
Full list of author information is available at the end of the article

Taylor *et al. EJNMMI Research* (2017) 7:101

Page 2 of 11

In comparison, the rate at which tracer diffuses across a distance l through the extravascular space of tissue scales as

$$k_{\mathrm{eq}} \sim D/l^2, \tag{2}$$

where D is the diffusivity of the tracer. For FAZA and similarly sized molecules (on the order of several hundred Daltons), $D \sim 10 \ \mu\mathrm{m}^2/\mathrm{s}$ in most tissue [6, 7]. Hence, taking $l \sim 100 \ \mu\mathrm{m}$ to be the distance between capillaries, the equilibration rate $k_{\mathrm{eq}} \sim 20 \ \mathrm{h}^{-1}$ for tracer is typically much faster than the binding rate, and comparable to the rate of extravasation, k_1.

On the other hand, for tissue with substantial mucous deposits (common in carcinomas [8] such as pancreatic ductal adenocarcinoma [9]), where diffusivity can be slowed by two or more orders of magnitude [10, 11], the rate of equilibration slows drastically, becoming comparable to the binding rate. This can also happen in tissue with necrotic regions ($l \gtrsim 500 \ \mu\mathrm{m}$) interspersed with hypoxic cells.

Slow diffusive equilibration has two important consequences for quantifying tumour hypoxia based on tracer uptake. First, if an imaging voxel contains both hypoxic cells and either mucous or small necroses, the voxel-scale TBR value will be reduced by the fact that tracer does not reach diffusive equilibrium at the standard imaging time, between 2 and 3 h post-injection. Hence, the sensitivity of static PET imaging to hypoxia is diminished. Second, as tracer slowly equilibrates in mucinous and necrotic tissue, its concentration increases at a rate comparable to that due to hypoxia-induced binding and a compartment model [12–15] may not be able to distinguish the two processes. In this case, we hypothesize that the trapping rate k_3 represents a sum of the binding rate k_{b} and the rate of equilibration. Quantifying hypoxia based on k_3 will thus overestimate its extent since $k_3 \geq k_{\mathrm{b}}$.

In this paper, we seek to test these hypotheses by modeling the pharmamcokinetics of FAZA in 20 patients with pancreatic ductal adenocarcinoma (PDAC), applying basic principles of diffusive equilibration to interpret transport data calculated from a standard two-tissue compartment model.

Methods

Patient population and PET/CT scans

Data was taken from 20 patients with biopsy-confirmed pancreatic ductal adenocarcinoma and FAZA-PET scans. Dynamic PET imaging scans were acquired over 1 h following injection of FAZA. The 1-h time-activity curves (TAC$_1$) were each binned into 34 frames: 12 10-s frames, followed by 8 32-s frames, followed by 7 2-min frames, followed by 7 5-min frames. Patients returned for a static PET scan at 2 h. CT scans used for co-registration were taken at the beginning of the dynamic and static

PET scans. Further details of this patient cohort and the PET/CT scans have been described previously [16].

Region of interest contours

PET activity data was obtained for regions of interest (ROIs) contoured using co-registered CT images. Tumour ROIs were contoured by a radiologist using the CT scan at 2 h. This was co-registered manually to the initial CT scan and the two CT ROI sets were co-registered to the dynamic and static PET scans. In order to minimize effects resulting from high liver uptake of FAZA, aorta ROIs were contoured from the same range of PET/CT slices (along the cranial-caudal axis) as the tumour ROIs. At the level of the pancreas, the aorta is between 1.5 and 2 cm in diameter; to minimize partial volume effects, ROIs in the aorta were restricted to 0.75 cm in diameter and combined so that at least 25 PET voxels ($3.9 \times 3.9 \times 3.3$ mm^3 each) were imaged.

Compartment model analysis

Dynamic PET TACs of FAZA were analyzed using the two-tissue compartment model [12–15, 17–19]:

$$\frac{dC_d(t)}{dt} = k_1 C_{\mathrm{In}}(t) - [k_2 + k_3] \, C_d(t) \tag{3}$$

and

$$\frac{dC_b(t)}{dt} = k_3 C_d(t). \tag{4}$$

Here, the concentration of tracer in the extravascular space of an imaged region has been partitioned into an unbound, diffusing component C_d as well as a component C_b that is bound by hypoxia. C_{In} is the "input" function, which we took to be the imaged tracer concentration in the aorta, as described above. As noted earlier, k_1 and k_2 are the vascular influx and efflux coefficients and k_3 is the tracer trapping rate. The total tracer concentration in an imaged region is

$$C(t) = v_b C_{\mathrm{In}}(t) + (1 - v_b) \, [C_d(t) + C_b(t)] \,, \tag{5}$$

where v_b is the volume fraction occupied by blood in the region of interest.

The above model was fitted to both the 1-h TACs (TAC$_1$) as well as the combined 2-h TACs (TAC$_2$) comprising the 1-h TACs plus static scans at 2 h (in part to asses co-registration errors, which should be greater for TAC$_2$). Coefficients (v_b, k_1, k_2, and k_3) were determined by minimizing

$$\chi^2 = \sum_i^N w_i \left[C_{\mathrm{model}}(t_i) - C_{\mathrm{data}}(t_i) \right]^2, \tag{6}$$

where $C_{\mathrm{model}}(t_i)$ are the model activity values [Eqs. (3)–(5)] and $C_{\mathrm{data}}(t_i)$ are the measured values acquired during the N discrete time frames; $N = 34$ for TAC$_1$ and $N = 35$

Taylor *et al. EJNMMI Research* (2017) 7:101

Page 3 of 11

for TAC$_2$. To avoid over-weighting short-duration early time frames, we used the weighting function $w_i = \delta t_i$ in Eq. 6, where δt_i was the duration of the ith time frame (because the $t = 2$ h time-point in TAC$_2$ did not represent a true 1-h time bin beyond the TAC$_1$ data set, we used $\delta t_{35} = \delta t_{34} = 5$ min). Equation 6 was minimized in Wolfram Mathematica 11.1 using its built-in numerical minimization routine (NMinimize) with $C_{\text{model}}(t_i)$ calculated using trapezoidal integration.

An important tissue transport quantity is the *distribution volume*:

$$v_d \equiv \frac{k_1}{k_2 + k_3}. \tag{7}$$

It represents the volume fraction of an imaged ROI in which tracer initially fills; i.e., rapidly equilibrates in. Patlak's formula [20, 21],

$$\text{TBR}(t) = v_b + (1 - v_b)v_d + K_i(1 - v_b)\frac{\int_0^t d\tau\, C_{\text{In}}(\tau)}{C_{\text{In}}(t)}, \tag{8}$$

for the tumour-to-blood ratio at time t was used to "correct" TBR for distribution volume effects:

$$\begin{aligned} \text{TBR}_{\text{corrected}}(t) &\equiv \frac{\text{TBR}(t) - v_b(1 - v_d)}{v_d} \\ &= 1 + k_3(1 - v_b)\frac{\int_0^t d\tau\, C_{\text{In}}(\tau)}{C_{\text{In}}(t)}. \end{aligned} \tag{9}$$

In Eq. (8), $K_i \equiv k_3 v_d$ is sometimes referred to as the "net trapping rate". TBR$_{\text{corrected}}$ represents the theoretical tumour-to-blood ratio that would have arisen had the distribution volume been unity.

Correlations were analyzed between k_3, v_d, TBR, and TBR$_{\text{corrected}}$, where TBR was calculated as

$$\text{TBR}(t) \equiv \frac{C_{\text{data}}(t)}{C_{\text{In}}(t)} \tag{10}$$

at both $t = 1$ and 2 h. Pearson correlation coefficients were calculated to quantify correlations between voxel- and tumour-scale values of these quantities. Voxel-scale coefficients were calculated by fitting the above model to the individual TACs for each voxel, while tumour-scale values were obtained using the average TAC in each tumour. Correlations were reported as the population average (over twenty tumours) of the intra-tumour voxel-scale r values ("voxel-scale") and as correlations between tumour-scale values ("tumour-scale").

Results

Correlations between TBR and k_3

Comparing voxel-scale k_3 and TBR values in each tumour, weak correlations were found at 1 h (average of voxel-scale

r values $= 0.10$) and at 2 h (r value $= 0.01$). Patient-specific results are shown in Online Resource 1 (Additional file 1). Strong correlations were found between voxel-scale k_3 and TBR$_{\text{corrected}}$ at 1 h (population average r value $= 0.80$) and moderate correlations were found at 2 h (r value $= 0.53$). Although standard imaging protocols call for measurement of TBR at least 2 h after tracer injection, transport coefficient (v_b, k_1, k_2, k_3) values obtained using the 1- and 2-h data sets were equivalent to within fit errors to the compartment model. The reduction in correlations is thus a metric for co-registration errors between the 1- and 2-h data sets, as well as the diminished validity of Eq. (8), which is only a good approximation at times less than the equilibration time $1/k_{\text{eq}}$ [21]. Representative voxel-scale correlations are shown in Figs. 1a–d for one patient. Table 1 displays population averages of voxel-scale correlations using the 2-h data sets as well as the mean values of the corresponding quantities.
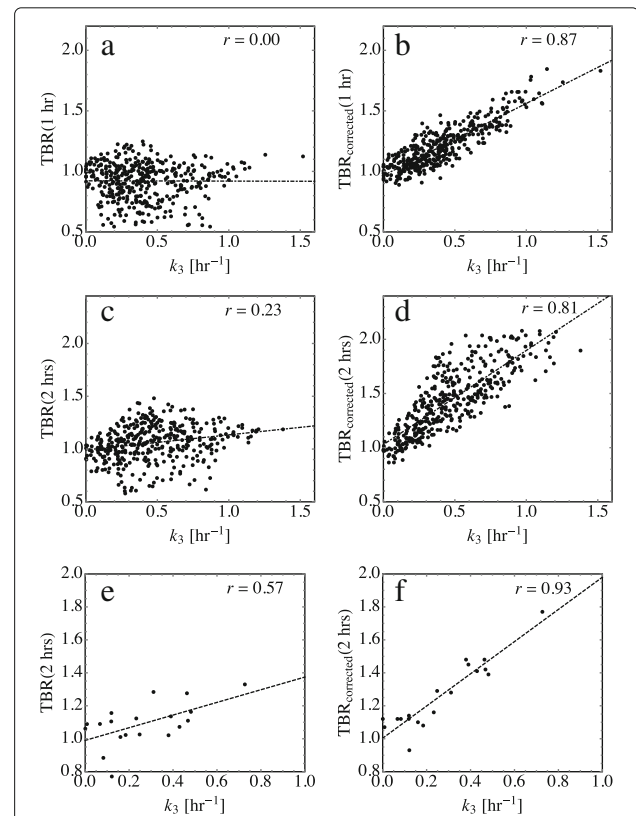
Fig. 1 Correlations between tumour-to-blood uptake ratios and the trapping rate are enhanced when uptake is corrected for the distribution volume. Left side: tumour-to-blood uptake ratio of FAZA versus trapping rate; right: tumour-to-blood uptake ratio corrected for the distribution volume versus trapping rate. **a** and **b** voxel-scale values for a representative patient tumour (pt. 2) using TAC$_1$. **c** and **d** same as **a** and **b** but with TAC$_2$. **e** and **f** Tumour-scale values using TAC$_2$ for all 20 tumours. Pearson correlation coefficients are shown

Taylor *et al. EJNMMI Research* (2017) 7:101

Page 4 of 11

Table 1 Top: Correlation matrix of Pearson correlation coefficients between the mean voxel-scale parameters across the twenty tumours studied using the 2-h data sets. Bottom: Population average values of the corresponding voxel-scale coefficients. Standard deviations of mean values across patients are indicated in parentheses

	$k_3\,[\mathrm{h}^{-1}]$	v_d	TBR	TBR$_{\text{corrected}}$
k_3	–	−0.59	0.01	*0.52*
v_d	−0.59	–	0.35	−0.58
TBR	0.01	0.35	–	0.50
TBR$_{\text{corrected}}$	*0.52*	−0.58	0.50	–
	$k_3\,[\mathrm{h}^{-1}]$	v_d	TBR	TBR$_{\text{corrected}}$
	0.30 (0.20)	0.85 (0.10)	1.06 (0.13)	1.25 (0.20)

Whole-tumour kinetics are less sensitive to co-registration errors and tumour-scale trapping rate exhibited modest correlations with TBR (across twenty patients, mean r = 0.58) but strong correlations with TBR$_{\text{corrected}}$ (mean r = 0.93); see Fig. 1e, f and Table 2. Mean tumour-scale values of k_3, v_d, TBR, and TBR$_{\text{corrected}}$ were identical to the values shown in Table 1 to within a few percent.

Relationship between v_d and k_3

In all patients, voxel-scale k_3 values were found to depend strongly on v_d (population average of voxel-scale r-values = -0.59; see Table 1), with k_3 increasing as v_d decreases. Figures 2a and d show two representative examples. Parametric maps of a transverse slice in each of these patients are shown in Fig. 3. Tumour-scale correlations between v_d and k_3 are reduced ($r = -0.34$) but still substantial; see Table 2.

To account for the unexpected correlations between k_3 and v_d, we propose a model (shown schematically in Fig. 4) in which an imaged voxel is comprised of two tissue types: one in which tracer reaches diffusive equilibrium rapidly (with concentration $C^{(r)}$), and one in which it reaches equilibrium slowly (with concentration $C^{(s)}$):

$$C_d(t) = v_s C_d^{(s)}(t) + (1 - v_s) C_d^{(r)}(t). \qquad (11)$$

Here, v_s represents the voxel volume fraction in which tracer is slow to equilibrate. As noted in the Introduction,

Table 2 Correlation matrix of Pearson correlation coefficients between the tumour-scale parameters across the twenty tumours studied using the 2-h data sets

	k_3	v_d	TBR	TBR$_{\text{corrected}}$
k_3	–	−0.34	*0.58*	*0.93*
v_d	−0.34	–	0.30	−0.26
TBR	*0.58*	−0.26	–	*0.66*
TBR$_{\text{corrected}}$	*0.93*	−0.26	*0.66*	–

tracer will equilibrate slowly in mucinous and necrotic tissue owing to the slow diffusivity and long diffusive distances, respectively.

Having defined the above sub-compartments, the distributed-parameter compartment model [22] that describes the effects of having regions of slow-equilibration is

$$\frac{dC_d^{(r)}(t)}{dt} = \frac{k_1}{1 - v_s}\left[C_{\text{In}}(t) - C_d^{(r)}(t)\right]$$
$$- \left(k_{\text{b}} + \frac{k_{\text{eq}} v_s}{1 - v_s}\right) C_d^{(r)}(t) + \frac{k_{\text{eq}} v_s}{1 - v_s} C_d^{(s)}(t), \qquad (12)$$

$$\frac{dC_d^{(s)}(t)}{dt} = k_{\text{eq}}\left[C_d^{(r)}(t) - C_d^{(s)}(t)\right], \qquad (13)$$

and

$$\frac{dC_b(t)}{dt} = k_{\text{b}} C_d^{(r)}(t). \qquad (14)$$

The factors of $1 - v_s$ and v_s here ensure detailed balance amongst the compartments. k_{b} is the binding rate due to hypoxia and k_{eq} represents the equilibration rate in the regions of slow-equilibration. Recall from the Introduction that we expect it to be on the order of $(0.1 \rightarrow 1)$ h^{-1} when equilibration is driven by diffusion; see Eq. (2). In writing Eq. (14), it has been assumed that tracer does not bind inside regions of slow-equilibration since, e.g., necrotic cells and extracellular mucous deposits do not bind hypoxia-PET nitroimidazole tracers [12].

At times $k_1^{-1} \lesssim t \ll k_{\text{eq}}^{-1}$, after diffusive equilibration is achieved in the rapidly equilibrating regions $\left[C_d^{(r)}(t) \simeq C_{\text{In}}(t)\right]$ but not yet in the slow-equilibrating regions, the tissue-to-blood ratio is readily obtained by integrating Eqs. (12)–(14):

$$\text{TBR}(t) \simeq v_b + (1 - v_b)(1 - v_s)$$
$$+ \left(k_{\text{b}} + \frac{k_{\text{eq}} v_s}{1 - v_s}\right)(1 - v_b)(1 - v_s)\frac{\int_0^t d\tau\, C_d^{(r)}(\tau)}{C_{\text{In}}(t)}. \qquad (15)$$
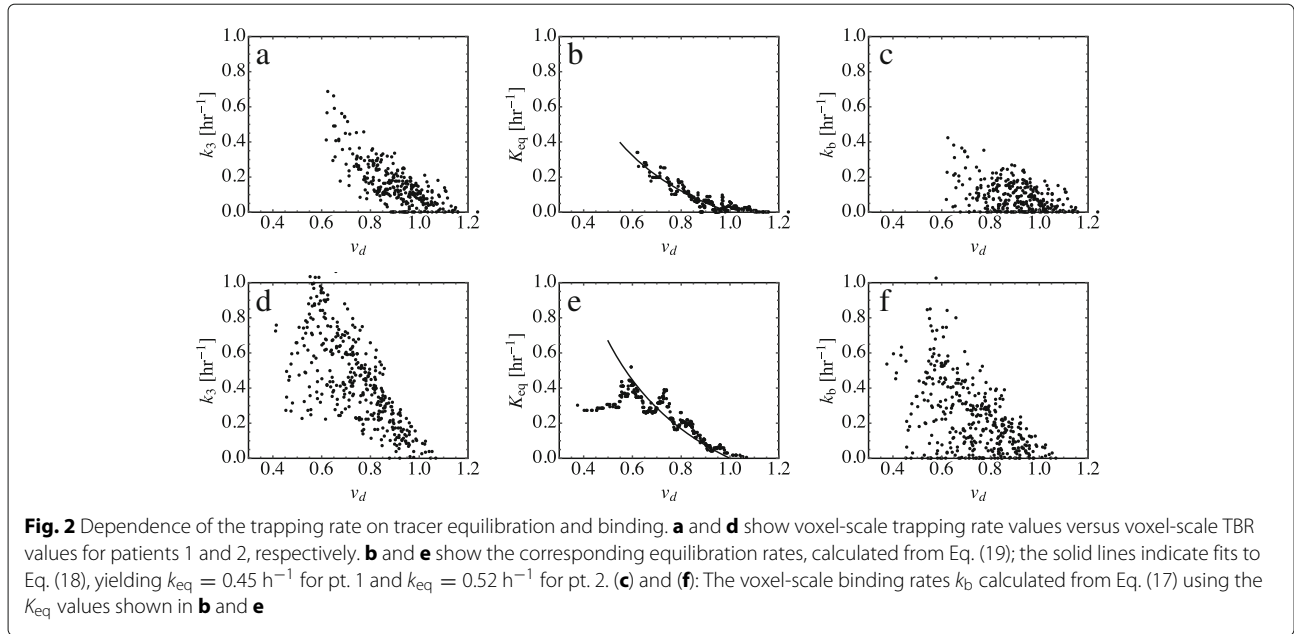
In arriving at this result, we have neglected back-flux from the slow-diffusion region, dropping the contribution arising from $C_d^{(s)}$ in Eq. (13). This is valid as long as $t \lesssim k_{\text{eq}}^{-1}$.

Since $C_d^{(r)}(t) \rightarrow C_{\text{In}}(t)$ for $t \gtrsim k_1^{-1}$, Eq. (15) is identical to the Patlak result Eq. (8), with

$$v_s = 1 - v_d. \qquad (16)$$

and

$$k_3 = k_{\text{b}} + \frac{k_{\text{eq}}(1 - v_d)}{v_d} \equiv k_{\text{b}} + K_{\text{eq}}(v_d), \qquad (17)$$

Taylor *et al. EJNMMI Research* (2017) 7:101

Page 5 of 11

Fig. 2 Dependence of the trapping rate on tracer equilibration and binding. **a** and **d** show voxel-scale trapping rate values versus voxel-scale TBR values for patients 1 and 2, respectively. **b** and **e** show the corresponding equilibration rates, calculated from Eq. (19); the solid lines indicate fits to Eq. (18), yielding $k_{eq} = 0.45$ h^{-1} for pt. 1 and $k_{eq} = 0.52$ h^{-1} for pt. 2. (**c**) and (**f**): The voxel-scale binding rates k_b calculated from Eq. (17) using the K_{eq} values shown in **b** and **e**

where we have defined

$$K_{eq}(v_d) \equiv k_{eq}(1 - v_d)/v_d. \qquad (18)$$

Equations (16) and (17) are our main theoretical results. They show that the distribution volume v_d defined in Eq. (7) is the volume fraction of tissue in which tracer rapidly equilibrates and that the standard two-tissue compartment model trapping rate in general represents the sum of the rate of binding due to hypoxia and the equilibration rate. In turn, this means that it is not possible to distinguish binding from equilibration from just the shape of the time-activity curves.

To distinguish k_b and K_{eq} in k_3, voxel-scale k_3 values were arranged into bins based on distribution volume values. Because there will always be a cohort of normoxic voxels in a tumour for which $k_b = 0$ (unless the hypoxic fraction is unity, simple Poissonian statistics dictates as much), it is assumed that the lowest M values of k_3 in these
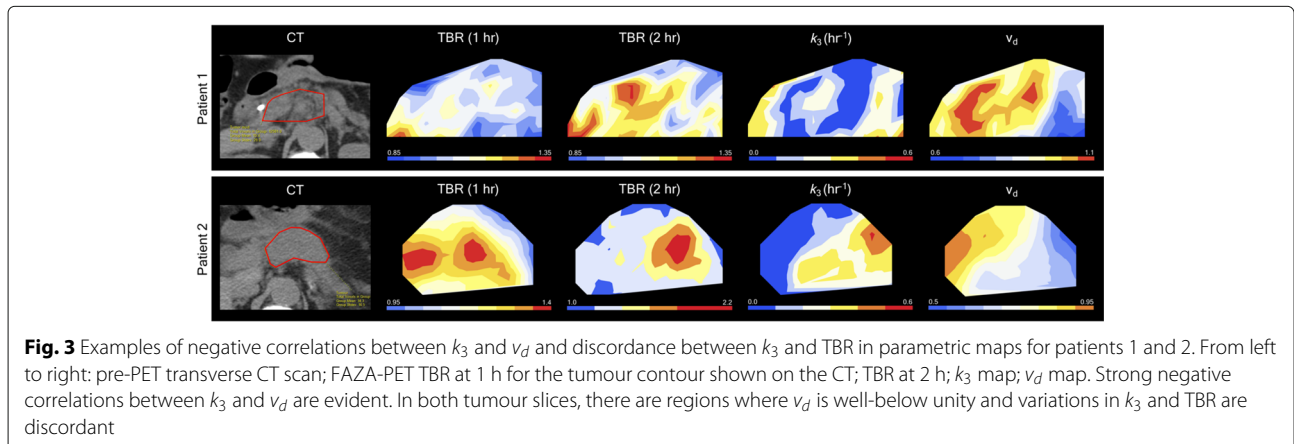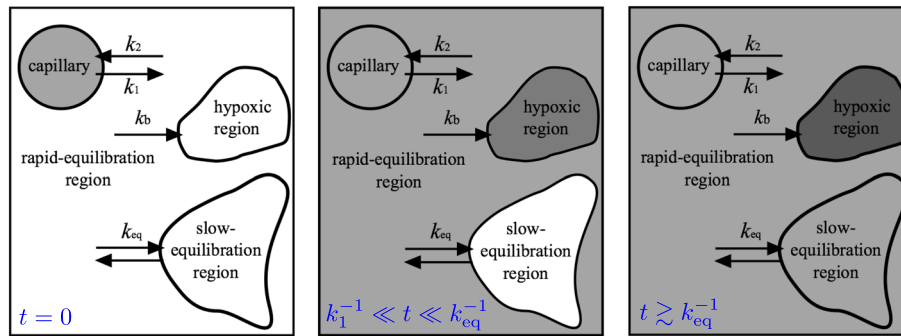
bins represent equilibration:

$$K_{eq}\left[(v_d)_i\right] = \frac{1}{M} \sum_{j=1}^{M} \min \left[\{k_3\}_{(v_d)_i}\right]_j. \qquad (19)$$

Equation (19) is strictly valid in the limit where the variance in k_{eq} values is much smaller than the variance in k_b values (so that the two distributions can be distinguished). The choice of M is dictated by their relative sizes:

$$\frac{M}{N_b} = \frac{\left(\sigma_{k_{eq}} / k_{eq}\right)}{\sqrt{\left(\sigma_{k_{eq}} / k_{eq}\right)^2 + \left(\sigma_{k_b} / k_b\right)^2}}, \qquad (20)$$

where N_b is the total number of values within each bin, σ_X and X denote the standard deviation and mean values of $X = k_b$ or k_{eq}. Assuming that the relative variance $\left(\sigma_{k_b} / k_b\right)$ is equal to that for the oxygen partial

Fig. 3 Examples of negative correlations between k_3 and v_d and discordance between k_3 and TBR in parametric maps for patients 1 and 2. From left to right: pre-PET transverse CT scan; FAZA-PET TBR at 1 h for the tumour contour shown on the CT; TBR at 2 h; k_3 map; v_d map. Strong negative correlations between k_3 and v_d are evident. In both tumour slices, there are regions where v_d is well-below unity and variations in k_3 and TBR are discordant

Taylor *et al. EJNMMI Research* (2017) 7:101

Page 6 of 11

Fig. 4 Schematic of our partitioning model. From left to right: at $t = 0$ (left panel), tracer (gray-filled regions) is only in the capillary; for $k_1^{-1} \ll t \ll k_{eq}^{-1}$ (middle panel), tracer fills the rapid-equilibration regions and begins to bind where hypoxia arises; for $t \gtrsim k_{eq}^{-1}$ (right panel), tracer fills all regions, including the slow-equilibration regions that occupy a volume fraction v_s of the region of interest

pressure P_{O_2} (the case, e.g., when the two are related by a Michaelis-Menten-type relation [12]), the variance in k_b is expected to be large, based on the broad distribution of P_{O_2} levels in tumours: $\left(\sigma_{P_{O_2}} / P_{O_2} \right) \gtrsim 1$ [23]. In contrast, the relative variance in k_{eq}—reflecting that of the size l of the regions in which tracer is slow to equilibrate—is small. This was estimated by calculating the variance in the minimum k_3 value in each bin with respect to a v_d-dependent average (see, e.g., the curve fits in Fig. 2). Across our twenty patients, we found an average value $\left(\sigma_{k_{eq}} / k_{eq} \right) \sim 0.4$. As a compromise to having a sufficient number of voxels to ensure the validity of statistics and few enough to have sufficient resolution in v_d-space to carry out these curve fits, bins were chosen to contain ten voxels. Hence, we chose $M = 0.4 \times 10 = 4$. A sensitivity analysis of the predicted equilibration rates and the choice of M is presented in Online Resource 2 (Additional file 2).

An example of this algorithm is shown for two patients in Figs. 2 and 5. Voxel-scale values of K_{eq} in each of these bins as determined by Eq. (19) are plotted in Fig. 2b and e. The solid lines in this figure are fits to $K_{eq}(v_d) = k_{eq}(1 - v_d)/v_d$. (The poor fit in Fig. 2e for $\lambda \lesssim 0.6$ may be due to a percolation effect: for distribution volumes less than ~ 0.65, regions of slow equilibration begin to overlap [24] and v_d will become dependent on the mean size l of these regions. Hence, from Eq. (2), k_{eq} will also begin to depend on v_d). Also shown in Fig. 2c and f are the voxel-scale binding rates determined from Eqs. (17) and (19). Figure 5 shows parametric maps of k_3, k_{eq} and k_b for the same tumour slices shown in Fig. 3.

The correlation matrix between derived voxel-scale parameters from our model is shown in Table 3 along with population averages of these parameters. The relative sizes of the correlations between k_3 and K_{eq} ($r = 0.57$) and k_b ($r = 0.86$) are measures of how much equilibration and binding were found to contribute to the net trapping rate

k_3. Most of the v_d dependence of k_3 is contained in K_{eq}, as evidenced by the strong correlations between v_d and K_{eq} ($r = -0.73$) but comparatively weak correlations k_b and v_d ($r = -0.27$). Not shown are correlations between these quantities and the vascular influx rate k_1 since these were small ($|r| < 0.15$) for all cases.

The v_d-dependence of k_3 in our model is a consequence only of mass conservation and the assumption that there exists a compartment in which tracer is slow to reach diffusive equilibrium. It does not depend on a specific microscopic model for equilibration. We tested the prediction given by Eq. (17) by fitting the binned K_{eq} values to a function of the form $K_{eq}(v_d, \gamma) = k_{eq} [(1 - v_d)/v_d]^\gamma$ to determine how close γ was to its predicted value of unity. Averaging over all tumours, we found $\gamma = (0.9 \pm 0.4)$, with the error given by the standard deviation of values across all tumours. This confirms that our model in which tracer equilibrates slowly in a fraction $1 - v_d$ of tissue is consistent with our data. The mean equilibration rate derived from these fits was $k_{eq} = 0.44 \, \mathrm{h}^{-1}$ (standard deviation of $0.29 \, \mathrm{h}^{-1}$ across all patients), corresponding to an equilibration time of $1/k_{eq} \sim 2.3 \, \mathrm{h}$.

Discussion

It is well-appreciated that the uptake of hypoxia-sensitive PET tracers is dependent on tissue transport properties as well as hypoxia [13, 14, 17, 18, 25]. In principle, dynamic PET modeling corrects for transport properties such as slow tissue diffusivity that can impede the uptake of tracer and reduce sensitivity to hypoxia when such features are co-localized with hypoxia in PET voxels. This is especially problematic since PET voxels are typically large enough $[\sim (4 \, \mathrm{mm})^3]$ to include diverse cell populations, with widely varying pathology [26]. The quantity of primary interest in a compartment model analysis of dynamic PET imaging is the trapping rate k_3, commonly believed to be sensitive to hypoxia via the underlying binding kinetics [12–14]. Static PET imaging is more feasible

Taylor *et al. EJNMMI Research* (2017) 7:101

Page 7 of 11
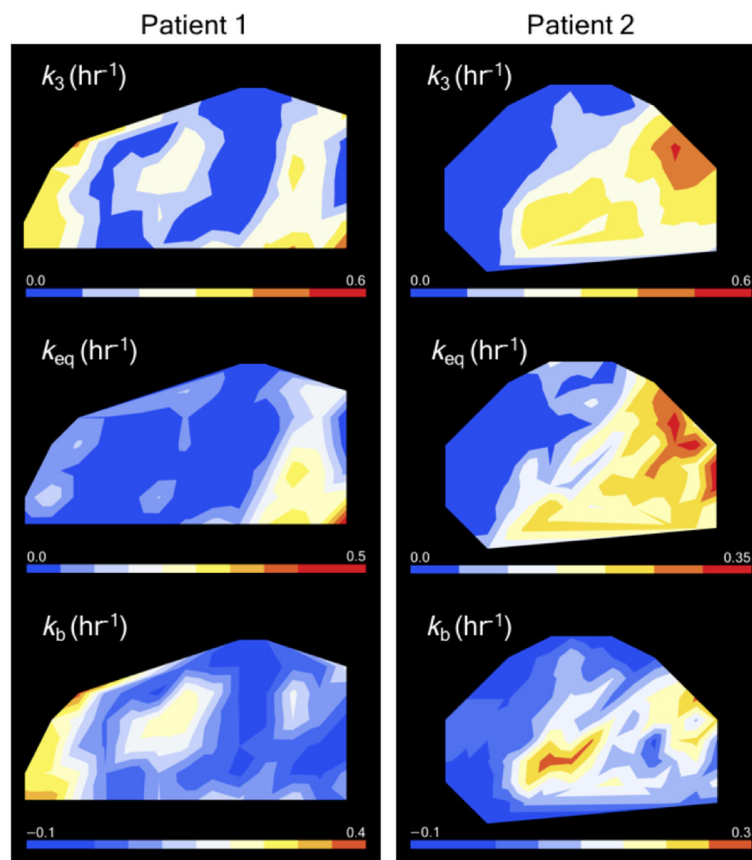
Fig. 5 Parametric maps for an axial tumour slice from patients 1 (left) and 2 (right) showing the spatial distribution of binding and equilibration rates
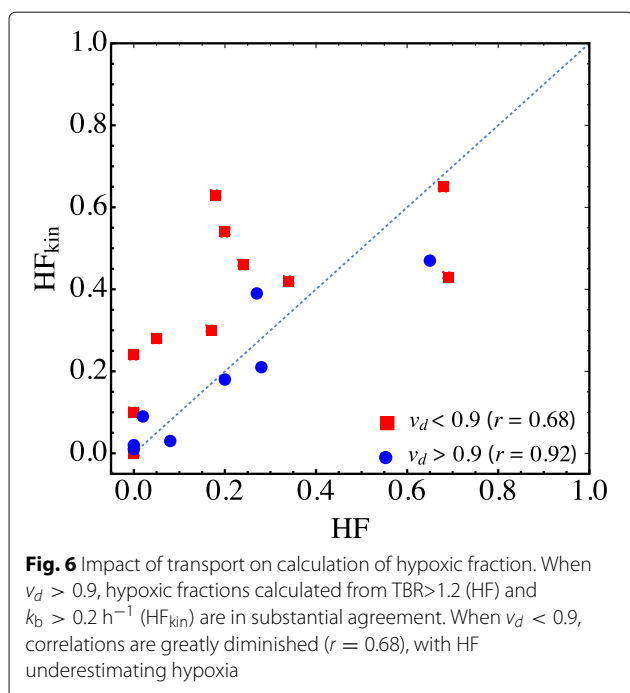
clinically, however, and it is often assumed that one can adopt static imaging in place of kinetic imaging when some appropriate uptake metric–SUV for FDG-PET or TBR for hypoxia-PET–is well-correlated with k_3 [27, 28].

Table 3 Top: Correlation matrix of Pearson correlation coefficients between the mean voxel-scale parameters across the twenty tumours studied using the 2-h data sets. Bottom: Population-averages of the corresponding voxel-scale rate coefficients; values are shown in units of h^{-1}. Standard deviations of mean values across patients are indicated in parentheses. Also shown is the population average k_{eq} value, which was calculated from fits to data from all voxels in each tumour, as described in the text

	k_3	K_{eq}	k_b	v_d
k_3	–	*0.57*	*0.86*	*−0.59*
K_{eq}	*0.57*	–	0.18	*−0.73*
k_b	*0.86*	0.18	–	*−0.27*
v_d	*−0.59*	*−0.73*	*−0.27*	–
	k_3	K_{eq}	k_b	k_{eq}
	0.30 (0.20)	0.17 (0.15)	0.14 (0.08)	0.44 (0.29)

In this paper, we have investigated dynamic and static PET in 20 patients with pancreatic adenocarcinoma (PDAC) and found k_3 values to be only modestly correlated with TBR. Using Patlak's formula to analyze these correlations, we found that a highly variable distribution volume across patients was primarily responsible for the reduced correlations, consistent with recent findings of FMISO kinetics in head and neck tumours [25].

Correcting for the distribution volume, correlations were considerably stronger and the corrected tumour-to-blood ratio was *increased* (see Fig. 1). This shows that tracer uptake at 2 h in these patients is sensitive both to hypoxia and tissue transport properties (distribution volume), with the result that variability in tissue transport properties *reduces* the sensitivity of static PET imaging to hypoxia. Figure 6 compares hypoxic fractions in the twenty tumours calculated using: a.) the fraction of voxels for which TBR>1.2 and b.) the fraction of voxels for which $k_b > 0.2$ h^{-1}, a threshold chosen such that the two hypoxic fractions agree when transport effects are small ($v_d > 0.9$). When transport effects are substantial ($v_d < 0.9$), correlations between the two methods of calculating hypoxic fractions are greatly reduced (*r* goes from 0.92 to

Taylor *et al. EJNMMI Research* (2017) 7:101

Page 8 of 11

Fig. 6 Impact of transport on calculation of hypoxic fraction. When $v_d > 0.9$, hypoxic fractions calculated from TBR>1.2 (HF) and $k_b > 0.2$ h^{-1} (HF$_{kin}$) are in substantial agreement. When $v_d < 0.9$, correlations are greatly diminished ($r = 0.68$), with HF underestimating hypoxia

0.68), with the TBR approach underreporting hypoxia on average.

At first glance, this would suggest that these tumours would benefit from dynamic PET imaging. The trapping rate was found to exhibit a strong dependence on the distribution volume, however, implying that k_3 describes both the binding rate due to hypoxia as well as the rate of equilibration. A model was developed to explain this in which the extravascular tissue space was divided into two regions, one in which tracer rapidly achieved diffusive equilibrium and one in which it equilibrated slowly. The population-averaged equilibration rate $k_{eq} \simeq (0.44 \pm 0.29)$ h^{-1} in the latter region is consistent with our estimate in the Introduction of having either mucinous regions (on the order of tens to hundreds of microns in extent) where diffusivity is greatly slowed or micronecroses, smaller than a PET imaging voxel but larger than $\sim 500\,\mu$m across.

The long equilibration time $\left[1/k_{eq} \sim 2.3\text{ h}\right]$ implied by this result means that unbound tracer will not equilibrate until well-after tracer injection, at times $t \gg 1/k_{eq}$. At this time, the concentration of tracer in both the slow- and fast-equilibrating regions will approach that in blood and the effect of the distribution volume on TBR will vanish. Ideally, static hypoxia-PET imaging would be carried out when $t \gg 1/k_{eq}$ in order to remove this sensitivity to transport. Unfortunately, the half-life of ^{18}F is short and imaging times are typically restricted to be 3 h or less. (In our study, it was felt that accrual would be challenged by imaging patients past 2 h.)

If slow equilibration were due to necroses, k_1–a measure of perfusion–would be correlated with k_{eq}. No such

correlations were found, leading us to hypothesize that mucous deposits comprised the regions of slow equilibration. Necroses are also rare in PDAC, whereas mucous gel-forming mucins are commonly over-expressed [9]. Amongst the twenty patients, the tumour volume fraction v_d in which tracer equilibrated rapidly varied from 0.68 to 1, with an average value of 0.85. This implies mucinous region volume fractions ranging from 0 to 30%, with an average value of 15%. Tumours were resected in four patients and examined by a pathologist [I.S.]. Although not a sufficient number to be able to definitively attribute the reduced distribution volume to mucous, the patients with the smallest and largest distribution volumes of this four exhibited significant and negligible mucin expression, respectively; see Fig. 7.

Our conclusion that equilibration is slow in parts of pancreatic tumours is not inconsistent with claims by us [21] and others [25] that *tumour-scale* equilibration rates are rapid. The characteristic equilibration rate in the fast-equilibrating regions can be approximated by k_1 which, even for the hypo-perfused PDAC tumours studied in this work, was fast compared to k_b and k_{eq}. The population average of the tumour-scale k_1 values was ~ 0.3 min^{-1} [16]. Regions of slow-equilibration occupy a relatively small fraction of the tumours and hence, the tumour-scale equilibration rate is not strongly affected by these.

Although we have proposed a scheme to differentiate binding from equilibration, and hence, to quantify hypoxic status via the surrogate binding rate k_b, the accuracy of this approach relies on the assumption that the variance in the equilibration rate is much smaller than the variance in the binding rate: $\left(\sigma_{k_{eq}} / k_{eq}\right) \ll \left(\sigma_{k_b} / k_b\right)$. Only then can we attribute the lowest few k_3 values in each v_d bin to K_{eq} and not k_b.

The fact that the estimated $\left(\sigma_{k_{eq}} / k_{eq}\right)$ was only marginally smaller than $\left(\sigma_{k_b} / k_b\right)$ means that our analysis did not completely distinguish equilibration and binding. In effectively assuming that the variance in the equilibration rate was zero, our analysis erred on the side of underestimating the equilibration rate and hence, overestimated the binding rate k_b. At the same time, our scheme still represents an improvement over hypoxia quantification using k_3 since k_3 will always be larger than our estimated k_b, which in turn is likely larger than the true k_b. Full validation of our approach will rely on comparing our estimates of k_b and oxygen levels using other methods such as immunohistochemical staining of resected tumours. We plan on doing this in the future.

Beyond hypoxia quantification, dynamic PET imaging reveals additional information about tumour physiology that may prove to be clinically important [13, 14, 25, 29].

Taylor *et al. EJNMMI Research* (2017) 7:101

Page 9 of 11
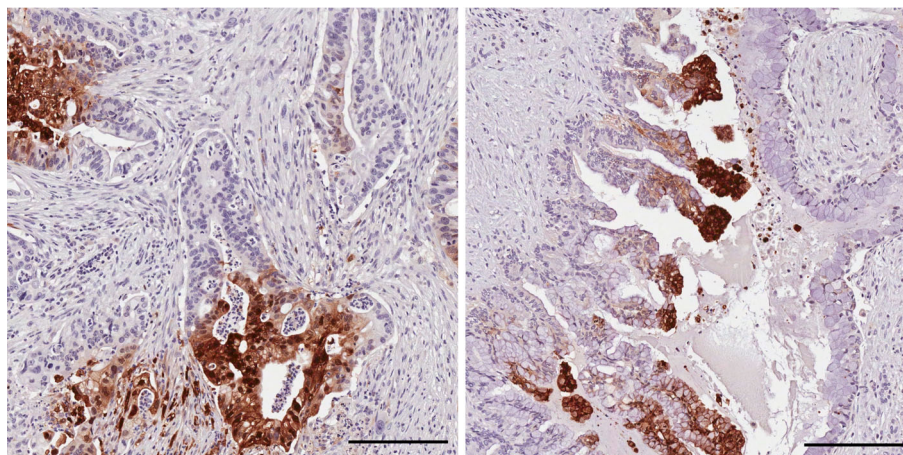
Fig. 7 Resected histology slices from two patients (16 and 17 in Online Resource 1 (Additional file 1)), illustrating the hypothesized dependence of the distribution volume on mucin expression. The tumour on the left exhibits little mucin while that on the right exhibits abundant apical mucin. The average distribution volumes for these tumours are 0.92 and 0.76, respectively, representing above- and below average levels. The black scale bars in the lower-right hand corners of these plots indicates a length of 200 μm; in comparison, a PET voxel is $\sim$4 mm across. Brown regions indicate staining for pimonidazole

In our case, we have found that the distribution volume of FAZA (and likely all freely-diffusible PET tracers) quantifies the amount of mucous present in pancreatic tumours. Over-expression of the mucous gel-forming mucin MUC5AC in PDAC is prognostic for shorter survival time [30], greater metastatic potential [9, 31], and immune system avoidance [32]. We hypothesize that the distribution volume in other tumour sites will likewise provide complementary physiological information beyond hypoxic status.

A key question raised by this work is whether or not the tissue transport effects identified here confound hypoxia quantification using other hypoxia-PET tracers such as FMISO and in other tumour sites. The primary impediment to tracer equilibration is slow diffusivity. FAZA has been estimated to diffuse marginally faster than FMISO [7], and so the issues identified here should impact FMISO to a comparable degree. Indeed, similar effects as the ones reported here have arisen in FMISO imaging of pre-clinical tumour models [33], as well as clinical pharmacokinetic studies of head and neck tumours [17, 25]. In all cases, a variable distribution volume diminished correlations between TBR and k_3. [The fact that $K_i = \nu_d k_3$ but not k_3 was found to be well-correlated with TBR in Ref. [33] can be understood from Eq. (8): K_i removes the variance in TBR arising from ν_d in the trapping term, but not the first two terms on the right-hand side of this equation.] In recent work, Grkovski et al. discuss the important role of the distribution volume in static PET hypoxia quantification and also report significant negative correlations between k_3 and ν_d [25]. The present work builds on these analyses by proposing a model in which k_3 is sensitive both to hypoxia-induced binding as well as diffusive equilibration of un-bound tracer.

Conclusions

The uptake of hypoxia-sensitive PET tracers in pancreatic tumours depends in a significant way on both tissue transport properties as well as the presence of hypoxia. Both dynamic- and static-PET based hypoxia surrogates—k_3 and TBR—are affected by regions where diffusive equilibrium is achieved very slowly, over several hours. We have proposed a scheme to extract the hypoxia-sensitive tracer binding rate as well as the from dynamic PET data and proposed this as a novel hypoxia biomarker. Our results are of relevance for all hypoxia-PET tracers and any tumour site where transport of small-molecular weight agents is challenged.

Additional files

Additional file 1: Table S1. (PDF 21 kb)

Additional file 2: Supplemental information. (PDF 100 kb)

Taylor *et al. EJNMMI Research* (2017) 7:101

Page 10 of 11

Authors' contributions

ET and JG carried out the compartment model analysis. ET, IY, HK, and MM developed the model used to analyze data. NCD, DWH, and DAJ participated in the design of the study. IS carried out the histology analysis. All authors read and approved the final manuscript.

Ethics approval and consent to participate

Consent for publication

Not applicable.

Competing interests

The authors declare that they have no competing interests.

Publisher's Note

Springer Nature remains neutral with regard to jurisdictional claims in published maps and institutional affiliations.

Author details

[1]Princess Margaret Cancer Centre, University Health Network, Toronto, Canada. [2]Techna Institute, University Health Network, Toronto, Canada. [3]Department of Medical Biophysics, University of Toronto, Toronto, Canada. [4]Department of Radiation Oncology, University of Toronto, Toronto, Canada. [5]Division of Medical Oncology and Hematology, Princess Margaret Cancer Centre, Toronto, Canada. [6]Department of Pathology, Hospital for Sick Children, Toronto, Canada. [7]Institute for Biomaterials and Biomedical Engineering, University of Toronto, Toronto, Canada.

References

1. Fleming IN, Manavaki R, Blower PJ, West C, Williams KJ, Harris AL, Domarkas J, Lord S, Baldry C, Gilbert FJ. Imaging tumour hypoxia with positron emission tomography. Brit J Cancer. 2015;112:238–50.
2. Rajendran JG, Krohn KA. F-18 fluoromisonidazole for imaging tumor hypoxia: imaging the microenvironment for personalized cancer therapy. Semin Nucl Med. 2015;45(2):151–62.
3. Koh WJ, Rasey JS, Evans ML, Grierson JR, Lewellen TK, Graham MM, Krohn KA, Griffin TW. Imaging of hypoxia in human tumors with [F-18] fluoromisonidazole. Int J Radiat Oncol Biol Phys. 1992;22(2):199–212.
4. Rajendran JG, Schwartz DL, O'Sullivan J, Peterson LM, Ng P, Scharnhorst J, Grierson JR, Krohn KA. Tumor hypoxia imaging with [F-18] fluoromisonidazole positron emission tomography in head and neck cancer. Clin Cancer Res. 2006;12(18):5435–41.
5. Muzi M, Peterson LM, O'Sullivan JN, Fink JR, Rajendran JG, McLaughlin LJ, Muzi JP, Mankoff DA, Krohn KA. 18F-Fluoromisonidazole Quantification of Hypoxia in Human Cancer Patients Using Image-Derived Blood Surrogate Tissue Reference Regions. J Nucl Med. 2015;56(8):1223–8.
6. Pruijn FB, Patel K, Hay MP, Wilson WR, Hicks KO. Prediction of tumour tissue diffusion coefficients of hypoxia-activated prodrugs from physicochemical parameters. Aust J Chem. 2008;61:687–93.
7. Wack LJ, Mönnich D, van Elmpt W, Zegers CML, Troost EGC, Zips D, Thorwath D. Comparison of [18F]-FMISO, [18F]-FAZA, and [18F]-HX4 for PET imaging of hypoxia—a simulation study. Acta Oncologica. 2015;54: 1370–1.
8. Lau SK, Weiss LM, Chu PG. Differential expression of MUC1, MUC2, and MUC5AC in carcinomas of various sites: an immunohistochemical study. Am J Clin Pathol. 2004;122(1):61–9.
9. Kaur S, Kumar S, Momi N, Sasson AR, Batra SK. Mucins in pancreatic cancer and its microenvironment. Nat Rev Gastroenterol Hepatol. 2013;10(10):607–20.
10. Georgiades P, Pudney PD, Thornton DJ, Waigh TA. Particle tracking microrheology of purified gastrointestinal mucins. Biopolymers. 2014;101(4):366–77.
11. Runnsjö A, Dabkowska AP, Sparr E, Kocherbitov V, Arnebrant T, Engblom J. Diffusion through Pig Gastric Mucin: Effect of Relative Humidity. PLoS ONE. 2016;11(6):e0157596.
12. Casciari JJ, Graham MM, Rasey JS. A modeling approach for quantifying tumor hypoxia with [F-18]fluoromisonidazole PET time-activity data. Med Phys. 1995;22:1127–39.
13. Thorwarth D, Eschmann SM, Paulsen F, Alber M. A kinetic model for dynamic [18F]-Fmiso PET data to analyse tumour hypoxia. Phys Med Biol. 2005;50:2209–24.
14. Thorwarth D, Eschmann SM, Scheiderbauer J, Paulsen F, Alber M. Kinetic analysis of dynamic 18F-fluoromisonidazole PET correlates with radiation treatment outcome in head-and-neck cancer. BMC Cancer. 2005;5:152.
15. Wang W, Georgi J-C, Nehmeh SA, Narayanan M, Paulus T, Bal M, O'Donoghue J, Zanzonico PB, Schmidtlein CR, Lee NY, Humm JL. Evaluation of a compartmental model for estimating tumor hypoxia via FMISO dynamic PET imaging. Phys Med Biol. 2009;54:3083–99.
16. Metran-Nascente C, Yeung I, Vines DC, Metser U, Dhani DC, Green D, Milosevic M, Jaffray D, Hedley DW. Measurement of tumor hypoxia in patients with advanced pancreatic cancer based on 18F-fluoroazomyin arabinoside uptake. J Nucl Med. 2016;57(3):361–6.
17. Wang W, Lee NY, Georgi J-C, Narayanan M, Guillem J, Schöder H, Humm JL. Pharmacokinetic Analysis of Hypoxia 18F-Fluoromisonidazole Dynamic PET in Head and Neck Cancer. J Nucl Med. 2010;51(1):37–45.
18. Bartlett RM, Beattie BJ, Naryanan M, Georgi J-C, Chen Q, Carlin SD, Roble G, Zanzonico PB, Gonen M, O'Donoghue J, Fischer A, Humm JL. Image-Guided PO2 Probe Measurements Correlated with Parametric Images Derived from 18F-Fluoromisonidazole Small-Animal PET Data in Rats. J Nucl Med. 2012;53(10):1608–15.
19. Wang K, Georgi J-C, Zanzonico P, Narayanan M, Paulus T, Bal M, Wang W, Cai A, O' Donoghue J, Ling CC, Humm JL. Hypoxia Imaging of Rodent Xenografts with 18F-Fluoromisonidazole: Comparison of Dynamic and Static PET Imaging. Int J Med Physics Clin Eng Radiat Oncol. 2012;1(3): 95–104.
20. Patlak CS, Blasberg RG, Fenstermacher JD. Graphical evaluation of blood-to-brain transfer constants from multiple-time uptake data. J Cereb Blood Flow Metab. 1983;3(1):1–7.
21. Taylor E, Yeung I, Keller H, Wouters BG, Milosevic M, Hedley DW, Jaffray DW. Quantifying hypoxia in human cancers using static PET imaging. Phys Med Biol. 2016;61:7957.
22. Larson KB, Markham J, Raichle ME. Tracer-kinetic models for measuring cerebral blood flow using externally detected radiotracers. J Cereb Blood Flow Metab. 1987;7(4):443–63.
23. Nordsmark M, Bentzen SM, Overgaard J. Measurement of human tumour oxygenation status by a polarographic needle electrode. An analysis of inter- and intratumour heterogeneity. Acta Oncol. 1994;33(4):383–9.
24. CD Lorenz, RM Ziff. Precise determination of the critical percolation threshold for the three-dimensional "Swiss cheese" model using a growth algorithm. J Chem Phys. 2011;114(8):3659–61.
25. Grkovski M, Schöder H, Lee NY, Carlin SD, Beattie BT, Riaz N, Leeman JE, O'Donoghue JA, Humm JL. Multiparametric Imaging of Tumor Hypoxia and Perfusion with 18F-Fluoromisonidazole Dynamic PET in Head and Neck Cancer. J Nucl Med. 2017;58:1072–80.
26. Busk M, Horsman MR, Overgaard J. Resolution in PET hypoxia imaging: Voxel size matters. Acta Oncologica. 2008;47(7):1201–10.
27. Freedman NM, Sundaram SK, Kurdziel K, Carrasquillo JA, Whatley M, Carson JM, Sellers D, Libutti SK, Yang JC, Bacharach SL. Comparison of SUV and Patlak slope for monitoring of cancer therapy using serial PET scans. Eur J Nucl Med Mol Imaging. 2003;30(1):46–53.
28. Doot RK, Dunnwald LK, Schubert EK, Muzi M, Peterson LM, Kinahan PE, Kurland BF, Mankoff DA. Dynamic and static approaches to quantifying 18F-FDG uptake for measuring cancer response to therapy, including the effect of granulocyte CSF. J Nucl Med. 2007;48(6):920–5.
29. Grkovski M, Lee NY, Schöder H, Carlin SD, Beattie BT, Riaz N, Leeman JE, O'Donoghue JA, Humm JL. Monitoring early response to chemoradiotherapy with 18F-FMISO dynamic PET in head and neck cancer. Eur J Nucl Med Mol Imaging. 2017;44(10):1682–91.
30. Takikita M, et al. Associations between Selected Biomarkers and Prognosis in a Population-Based Pancreatic Cancer Tissue Microarray. Cancer Res. 2009;69(7):2950–5.

Taylor *et al. EJNMMI Research* (2017) 7:101

Page 11 of 11

31. Yamazoe S, Tanaka H, Sawada T, Amano R, Yamada N, Ohira M, Hirakawa K. RNA interference suppression of mucin 5AC (MUC5AC) reduces the adhesive and invasive capacity of human pancreatic cancer cells. J Exp Clin Cancer Res. 2010;29:53.
32. Hoshi H, Sawada T, Uchida M, Saito H, Iijima H, Toda-Agetsuma M, Wada T, Yamazoe S, Tanaka H, Kimura K, Kakehashi A, Wei M, Hirakawa K, Wanibuchi H. Tumor-associated MUC5AC stimulates in vivo tumorigenicity of human pancreatic cancer. Int J Oncol. 2011;38(3): 619–27.
33. Busk M, Munk OL, Jakobsen S, Wang T, Skals M, Steiniche T, Horsman MR, Overgaard J. Assessing hypoxia in animal tumor models based on pharmocokinetic analysis of dynamic FAZA PET. Acta Oncol. 2010;49(7): 922–33.